AFRL-RY-WP-TR-2017-0198

NEW CONTENT ADDRESSABLE MEMORY (CAM) TECHNOLOGIES FOR BIG DATA AND INTELLIGENT ELECTRONICS ENABLED BY MAGNETO-ELECTRIC TERNARY CAM

Kang L. Wang

University of California, Los Angeles

DECEMBER 2017
Final Report

STINFO COPY

**AIR FORCE RESEARCH LABORATORY
SENSORS DIRECTORATE
WRIGHT-PATTERSON AIR FORCE BASE, OH 45433-7320
AIR FORCE MATERIEL COMMAND
UNITED STATES AIR FORCE**

NOTICE AND SIGNATURE PAGE

// Signature//   // Signature//
_____   _____
MARC P. HOFFMAN   KERRY L. HILL
Program Manager   Chief (acting)
Integrated Circuits & Microsystems Branch   Integrated Circuits & Microsystems Branch
Aerospace Components & Subsystems Division Aerospace Components & Subsystems Division

// Signature//
_____
JAMES M. SATTLER, Lt Col, USAF
Deputy
Aerospace Components & Subsystems Division
Sensors Directorate

REPORT DOCUMENTATION PAGE

Form Approved
OMB No. 0704-0188

The public reporting burden for this collection of information is estimated to average 1 hour per response, including the time for reviewing instructions, searching existing data sources, gathering and maintaining the data needed, and completing and reviewing the collection of information. Send comments regarding this burden estimate or any other aspect of this collection of information, including suggestions for reducing this burden, to Department of Defense, Washington Headquarters Services, Directorate for Information Operations and Reports (0704-0188), 1215 Jefferson Davis Highway, Suite 1204, Arlington, VA 22202-4302. Respondents should be aware that notwithstanding any other provision of law, no person shall be subject to any penalty for failing to comply with a collection of information if it does not display a currently valid OMB control number. **PLEASE DO NOT RETURN YOUR FORM TO THE ABOVE ADDRESS**.

1. REPORT DATE *(DD-MM-YY)*	2. REPORT TYPE	3. DATES COVERED *(From - To)*
December 2017	Final	9 August 2016 – 9 August 2017

4. TITLE AND SUBTITLE

NEW CONTENT ADDRESSABLE MEMORY (CAM) TECHNOLOGIES FOR BIG DATA AND INTELLIGENT ELECTRONICS ENABLED BY MAGNETO-ELECTRIC TERNARY CAM

5a. CONTRACT NUMBER
FA8650-16-1-7655

5b. GRANT NUMBER

5c. PROGRAM ELEMENT NUMBER
62716E

6. AUTHOR(S)

Kang L. Wang

5d. PROJECT NUMBER
N/A

5e. TASK NUMBER
N/A

5f. WORK UNIT NUMBER
Y1HU

7. PERFORMING ORGANIZATION NAME(S) AND ADDRESS(ES)

University of California, Los Angeles
11000 Kinross Ave, Suite 102
Los Angeles, CA 90095-1406

8. PERFORMING ORGANIZATION REPORT NUMBER

9. SPONSORING/MONITORING AGENCY NAME(S) AND ADDRESS(ES)

Air Force Research Laboratory, Sensors Directorate
Wright-Patterson Air Force Base, OH 45433-7320
Air Force Materiel Command
United States Air Force

Defense Advanced Research Projects Agency DARPA/MTO
675 North Randolph Street
Arlington, VA 22203

10. SPONSORING/MONITORING AGENCY ACRONYM(S)
AFRL/RYDI

11. SPONSORING/MONITORING AGENCY REPORT NUMBER(S)
AFRL-RY-WP-TR-2017-0198

12. DISTRIBUTION/AVAILABILITY STATEMENT
Approved for public release; distribution is unlimited.

13. SUPPLEMENTARY NOTES
This report is the result of contracted fundamental research deemed exempt from public affairs security and policy review in accordance with SAF/AQR memorandum dated 10 Dec 08 and AFRL/CA policy clarification memorandum dated 16 Jan 09. This material is based on research sponsored by Air Force Research laboratory (AFRL) and the Defense Advanced Research Agency (DARPA) under agreement number FA8650-16-1-7655. The views and conclusions contained herein are those of the authors and should not be interpreted as necessarily representing the official policies of endorsements, either expressed or implied, of AFRL and DARPA or the U.S. Government. Report contains color.

14. ABSTRACT

The Magneto-Electric Ternary Content Addressable Memory (MeTCAM) is a new associative memory based on the propagation of spikes. By removing redundant searches and only passing spikes where a match is found, this approach provides ultra-low energy search operations. To improve throughput, the in-array pipeline scheme has been developed, allowing the MeTCAM to operate at a higher frequency than its intrinsic search delay. Furthermore, the MeTCAM incorporates the state-of-the art nonvolatile memory device, the voltage-controlled magnetic tunnel junction (VC-MTJ), which not only reduces cell area (thus achieving higher density) but also eliminates standby energy. This report covers the technical details of the MeTCAM concept and supports the discussions by presenting simulation and analysis results that were developed under a DARPA funded effort. During the past year, advancements have been made on the design, verification, and implementation of the MeTCAM cell as well as the physical VC-MTJ device. Design and implementation challenges of the MeTCAM array are investigated and specific design guidelines are provided. Variations of the cell design are presented and evaluated. The results indicated a potential 90x improvement in the energy efficiency and a 50x improvement in the energy efficiency-throughput merit. Physical layout of the MeTCAM cell displays an area reduction of ~3x as compared to the conventional TCAM.

15. SUBJECT TERMS
magneto-electric ternary content addressable memory, voltage-controlled magnetic tunnel junction

16. SECURITY CLASSIFICATION OF:			17. LIMITATION OF ABSTRACT:	18. NUMBER OF PAGES	19a. NAME OF RESPONSIBLE PERSON (Monitor)
a. REPORT Unclassified	b. ABSTRACT Unclassified	c. THIS PAGE Unclassified	SAR	27	Marc P. Hoffman
					19b. TELEPHONE NUMBER *(Include Area Code)* N/A

Standard Form 298 (Rev. 8-98)
Prescribed by ANSI Std. Z39-18

Table of Contents

List of Figures

List of Tables

1. Introduction

1.1 Overview of TCAM

Content addressable memory (CAM) is one of the most promising hardware solution for high-speed data searching and has many practical applications such as anti-virus scanners, internet protocol (IP) filters, and network switches [1]. Since CAM stores the content (or data) in its internal memory elements and compares them with the search data in parallel, it can achieve much faster speed compared to the software lookup. There are two types of CAM: binary CAM and ternary CAM (TCAM). Especially, TCAM has not only two binary states ('0' and '1') but also an additional "don't care" state in which it performs the wild match. The most important qualification for a TCAM cell is fast operation speed for data searching. Due to this reason, static random access memory (SRAM) has been widely used in memory elements of the conventional TCAM cell, even though it has high bit-cell cost, typically requiring 12~16 transistors per cell as shown in Figure 1 [2], [3].
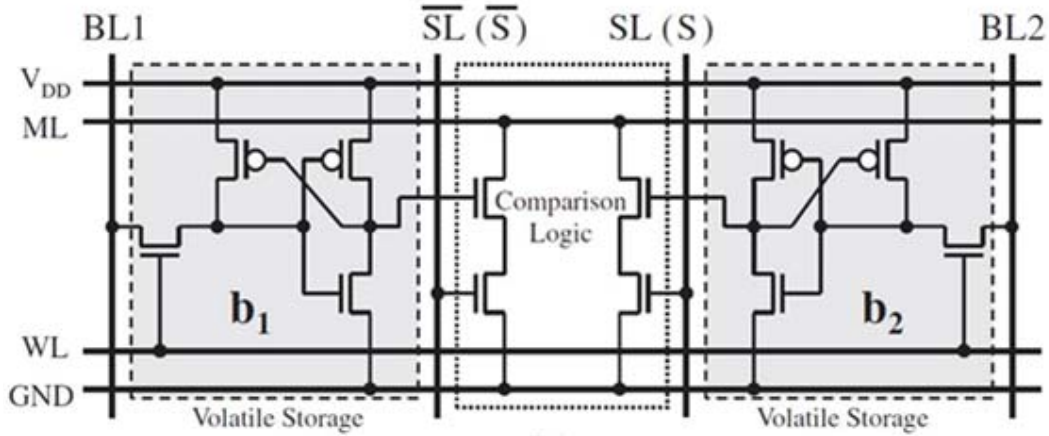
Figure 1: Conventional SRAM based TCAM Cell Architecture Consisting of Two Volatile Storage Elements and Comparison Logic [3]

However, recent trends in electronic applications, such as internet of things, big data, wireless sensors, and mobile devices, have begun to focus on the importance of energy consumption. The large SRAM-based TCAM cell inevitably increases capacitive loading of match lines (MLs) and search lines (SLs), which in turn raises dynamic power of search operation. Also, as complementary metal-oxide-semiconductor (CMOS) shrinks to nanometer-scale, the other major issue has emerged: a high standby power due to leakage current. A scaled-down channel length increases the leakage current, and hence the use of SRAM in TCAM applications is not a sustainable pathway.

1.2 Magneto-electric Random Access Memory (MeRAM) for TCAM Application

1.2.1 MeRAM Structure

The first approach to achieve a low power and high-density TCAM with a comparable searching speed is utilizing emerging memory technologies. Although emerging nonvolatile memories, such as resistive RAM (ReRAM), phase-change RAM (PCRAM), and spin-transfer RAM (STT-RAM) have been proposed for TCAM applications [3]–[5], we propose to use MeRAM as a memory element of TCAM because MeRAM outperforms other memory

1

technologies in terms of speed, energy, and density. Typically, a MeRAM cell consists of one transistor and one voltage-controlled magnetic tunnel junction (1T-1MTJ) as shown in Figure 2 where the bottom layer of the voltage-controlled magnetic tunnel junction (VC-MTJ) is connected to the drain of the access transistor, and the top layer is connected to the bit line (BL). The size of the access transistor in MeRAM can be reduced further in that the voltage-driven switching ideally does not require the flow of current. Thus the bit cell array of MeRAM can achieve higher density compared to other families of magneto-resistive RAM (MRAM). Also, the thickness of the tunnel barrier is relatively thick, practically reducing ohmic dissipation during the write operation.
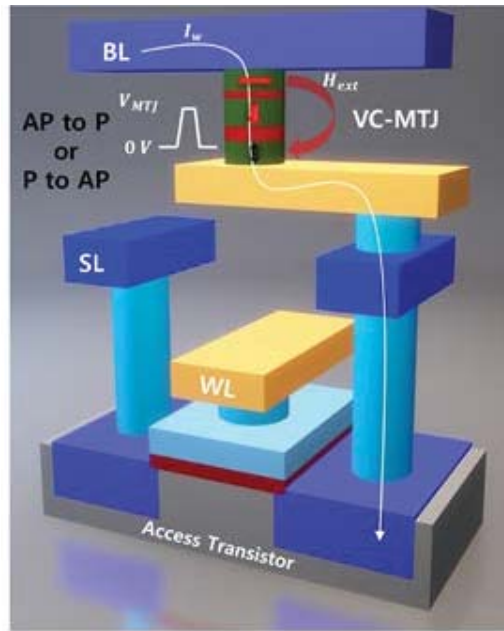
Figure 2: 1T-1MTJ Cell Architecture in MeRAM

Switching can be achieved by applying an electric pulse to the MTJ, which induces a magnetic precessional motion in the free layer. Since this type of switching mechanism is non-deterministic, a unipolar pulse can switch either from AP to P or from P to AP.

1.2.2 Voltage-Controlled Magnetic Tunnel Junction

Magnetic tunnel junctions (MTJs) are being actively developed by the semiconductor industry as one of the most promising memory devices, opening the door to new possibilities of next-generation low-power and high-speed system architectures. MTJs have compatibility with CMOS fabrication, sufficient on/off ratio (i.e. tunneling magneto-resistance (TMR)), and scalability. These characteristics allow MTJs interacting with the-state-of-the-art charge-based electronics on the same chip as a non-volatile storage block, leading to more compact, faster, and efficient electronics systems. An MTJ consists of two ferromagnetic layers (e.g. CoFeB) separated by a tunneling barrier (e.g. MgO). The magnetization of the pinned (or fixed) layer should not be changed under any bias conditions to achieve normal memory operations. Typically, two stable magnetic equilibrium exist along an easy magnetic axis in the free layer. The parallel state (P) occurs when the magnetic moments of the both layers are aligned in the same direction giving rise to a low resistance (R_P); on the other hand, the anti-parallel state (AP) occurs when the magnetic moment of the free layer is magnetized in the opposite direction to that of the pinned layer giving rise to a high resistance (R_{AP}). Note that

2

the MTJ can also have an intermediate resistance value between R_P and R_{AP} if the magnetization of the free layer has transient positions.

In the perpendicularly magnetized MTJ, the magnetization rotation between the $\hat{z}$ and $-\hat{z}$ directions occurs via traveling the in-plane (hard axis) by overcoming the energy barrier as shown in Figure 3. One of the most promising advantages of the perpendicular MTJ is that its energy barrier is not dominated by the geometry of the device but by the perpendicular anisotropy. Since the perpendicular anisotropy can be readily enhanced by engineering the interface effect, the perpendicular MTJ has a better scalability compared to that of the in-plane device governed by the aspect ratio. Recently, the large interfacial perpendicular anisotropy with a TMR ratio larger than 100% has been demonstrated in a Fe-rich CoFeB based MTJ [6]. More importantly, it has been experimentally observed that such perpendicular anisotropy can be modulated by applying electric fields across the MTJ device, resulting in a low-energy and high-speed voltage-controlled switching scheme.
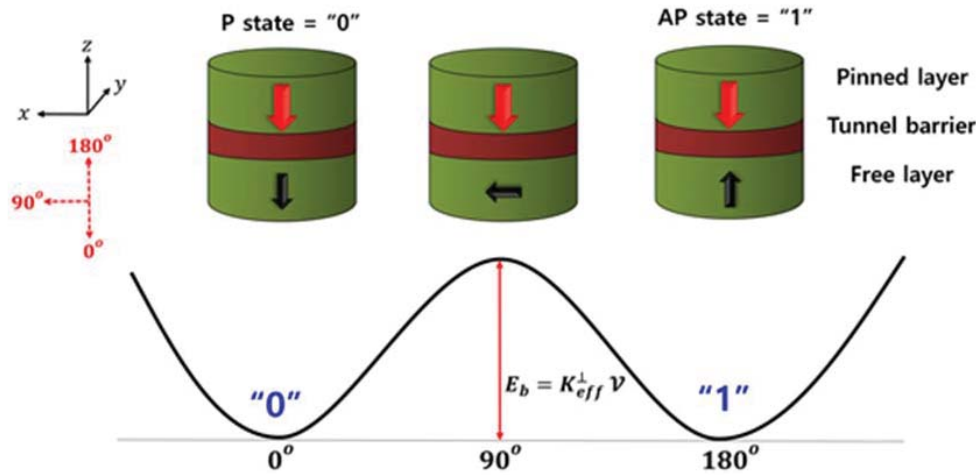
Figure 3: Perpendicular MTJ Utilizing the Interfacial Perpendicular Anisotropy for Creating Two Equilibrium States by Overcoming the Demagnetization Field in the $\hat{z}$ Directions
Since the shape anisotropy is not necessary for forming the energy barrier, the geometry of the device can be circular, leading to a better scalability.

1.3 MeTCAM Cell Structure and Operation

To design a low-standby power, high-speed accessibility, and low bit-cell cost TCAM cell, we propose a MeRAM based TCAM, referred to as MeTCAM. A MeTCAM cell consists of five transistors and two VC-MTJs, i.e. a 5T-2MTJ structure, as shown in Figure 4(a). M1 and M2 are comparison transistors whose gates are connected to the search lines (SL and SLB), and the drain are connected to the pinned layers of the MTJs if M1 and M2 are p-type metal-oxide-semiconductor (PMOS) transistors. M3 is an access transistor, which is required for the configuration (write) operation, and shared by two storage elements (MTJs), b1 and b2, to reduce the cell area. BFR is a digital inverter, which transfers a spike to the OUT node depending on the potential of the center (CE) node during the search operation. The truth table of MeTCAM cell for the search operation is shown in Table 1.
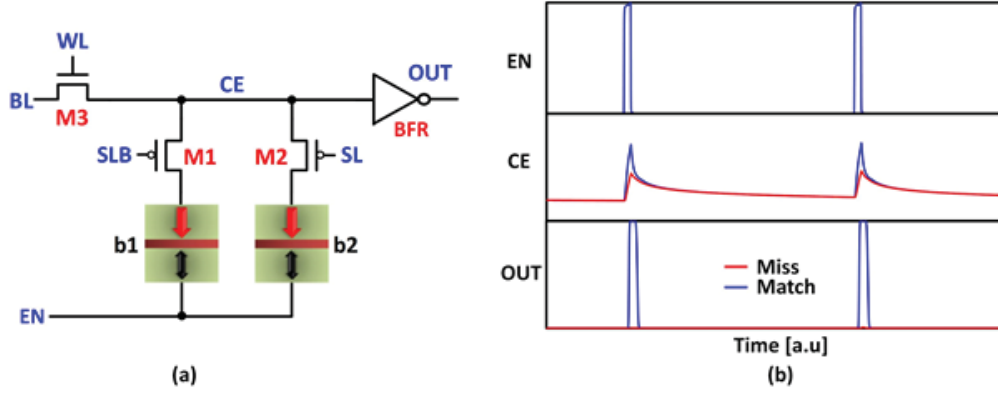
Figure 4: (a) Schematic and Search Operation of a MeTCAM Cell and (b) Circuit Simulation of Search Operation

When the cell receives a spike on enable (EN) node, the potential at CE rises. If the stored data matches the search data, the potential at CE will cross a threshold, which in turn transfers a spike to the post-cell via OUT node. On the other hand, in the mismatched case, the potential at CE will be lower than the threshold and there is no spiking at the OUT.

Table 1. Truth Table of MeTCAM Cell including Don't Care Condition
(In the case where M1 and M2 are PMOS)

Stored Data	(b1,b2)	$(\overline{SL}, SL)$	OUT
0	(0,1)	(1,0)	No Spike (Miss)
	(0,1)	(0,1)	Spike (Match)
1	(1,0)	(1,0)	Spike (Match)
	(1,0)	(0,1)	No Spike (Miss)
Don't care (X)	(0,0)	(1,0)	Spike (Match)
	(0,0)	(0,1)	Spike (Match)

In the configuration operation (write operation for MTJs), a two-step write method is used where writing of the memory elements b1 and b2 is performed in a serial manner. The pre-read step is necessary to deal with the non-deterministic behavior of the VCMA-driven precessional switching before the MTJ is written. Typically, a pulse with ~1 V amplitude and 1 ns duration should be applied to the MTJ to achieve precessional switching. To generate the write pulse in the proposed cell, the EN node is discharged to ground level, and M1 or M2 must be turned on to electrically connect between the CE node and EN node. Then, the write pulse applied to the BL is propagated to the CE node through M3.

The reduction of the cell area is achieved by using the shared access transistor M3 at the expense of configuration time. The increased configuration time is not a critical issue since the configuration operation of TCAM applications is not frequently performed compared to the search operation. Furthermore, the voltage-controlled magnetic anisotropy (VCMA)-driven precessional switching speed is fast enough to compensate for the increase in the number of the write operation.

In the search operation, the CE node is initially grounded as shown in Figure 4(b). When the cell receives a spike from the pre-cell via EN node, the potential of the CE node is determined by resistive-capacitive (RC) delay originating from the resistance of the MTJs

and the intrinsic capacitance of the CE node. For example, consider the case where the MeTCAM cell stores a logic value '0' (b1-R_P , b2-R_{AP}). In the case of a search '0' operation (SLB=0, SL=1), the CE node can reach the threshold voltage of the BFR transistor due to the relatively short RC delay through the low resistance of b1-R_P, resulting in generation of a spike on OUT node. On the other hand, for a search '1' operation (SLB=1, SL=0), the potential of the CE node is unable to reach the threshold of BFR due to the relatively long RC delay through the high resistance of b2-R_{AP}, causing no spike on OUT node. If the MeTCAM has a "don't care" condition (b1-R_P, b2-R_P), the cell generates a spike regardless of the search data due to the short RC delay.

1.4   Spike-based Architecture and Operation

The second approach to achieve a high-performance and low power MeTCAM can be realized by adopting a new architecture. The proposed MeTCAM cell receive a spike on its EN node to activate the comparison of the stored data with the search data. On the circuit level, instead of connecting all cells to a common ML, we connect the OUT node of each cell to the EN of the post cell. The implementation of this structure is shown in Figure 5.

When a search data arrives, a spike is passed to the EN of the first stage. The comparison result (OUT) of the first stage drives the EN of the second stage. If the search data matches the stored data, the search of the second stage is enabled, propagating the spike to the second stage. On the account of a mismatch, the mismatched cell does not generate a spike and all of the consecutive cells do not execute the search operation, since a spike will not arrive at the EN of the next cells. Figure 5 shows the concept of proposed spike-computation based MeTCAM.
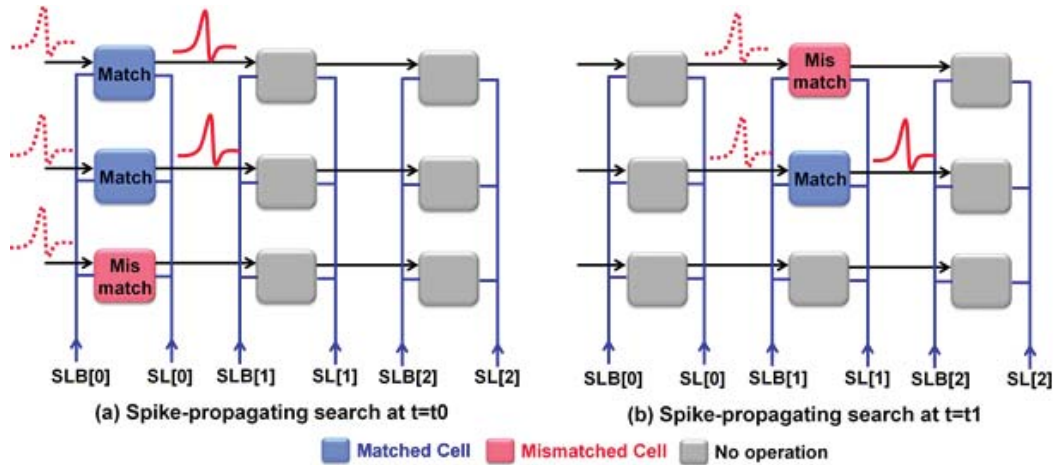
Figure 5: Concept of the Spike-Propagating Search
At t0, a spike is passed to the first stage. The spike propagates to the next stage if the search data is a match. At the mismatch, the spike stops. The pattern is a match if the spike arrives at the final stage.

By eliminating redundant searches, we have the advantage of serial search in terms of search energy/power density. The actual power is even smaller, since we do not need to drive a large loading on the shared ML. The stages are completely self-enabled, thus each stage does not require a control system to decide whether to disable the next stage. This allows the search speed to be only slightly slower than parallel search.

Pipelining has been widely adopted in computing to increase the overall throughput of a processor. However, conventional TCAM architectures cannot apply pipeline efficiently without splitting the array, adding additional registers, additional control systems, and degrading the performance of each stage due to the shared ML. If we attempt to start another search before the first one is finished, the two search results will collide on the ML, resulting in failure of both searches.

On the other hand, the spike-propagation architecture has a distinct OUT/EN for each stage, meaning that we can apply pipeline to increase throughput. Figure 6 shows how pipelining is applied to the spike-propagation architecture. As the spike passes to the second cell, the first cell is no longer occupied, thus we start a new search. In reality, this process is too fast to achieve full pipeline for every cell (K-stage pipeline for K-bit data). Peripheral circuits need calculation time and the search data (SL) needs settling time between each bit of search data. However, it is possible to apply pipeline when the spike has traveled a sufficient distance with the help of circuit techniques. In this work, we estimate that we can apply pipeline for every 16 cells (i.e. start a new search when the spike has arrived at the 16th cell), thus improving overall throughput by 8x for a 128-bit ML. This results in 0.125x average search time, and a search operation potentially even faster than completely parallel architectures.

	t=t0	t=t1	t=t2	t=t3
SL[0]	A[0]	B[0]	C[0]	D[0]
SL[1]	--	A[1]	B[1]	C[1]
SL[2]	--	--	A[2]	B[2]
SL[3]	--	--	--	A[3]

(a) Pipeline spike-propagating search at t=t3
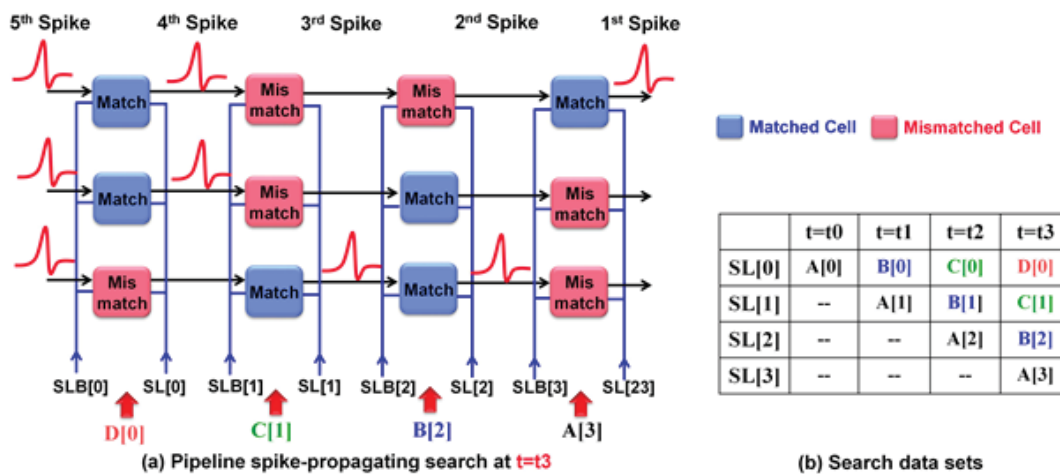
(b) Search data sets

Figure 6: Pipelining applied to the Spike-Propagation Architecture
(a) When the spike is passed to a later stage, the previous stage is free to accept another spike, and another search operation is started. (b) Processed data sets with respect to time. A, B, C, and D are different data sets. The pipeline scheme allows the array to fully use the resources (MeTCAM cells), increasing the throughput by a factor of P where P is the number of pipeline stage.

2. Calibration of VC-MTJ

2.1 Physical and Dynamic Model of VC-MTJ

A compact model accurately capturing the VCMA-induced magnetization dynamics is essential for successful development of VCMA-based memory. Although several works related to single-domain Landau-Lifshitz-Gilbert (LLG)-based macrospin models have been reported [7]–[10], a few have included the VCMA effect [11], [12]. It has been experimentally observed that the VCMA effect impacts magnetization dynamics both in the presence of STT, as well as on its own, giving rise to an oscillatory behavior of the switching probability as a function of applied pulse width, which differs from that of pure STT and thermally activated STT switchings. Hence, previous models need to be complemented by incorporating the voltage dependence of anisotropy at the interface of the free layer and the tunnel barrier.

In this chapter, we include the VCMA effect as a component of the effective magnetic field $\vec{H}_{eff}$ in an LLG-based macrospin compact model, allowing implementation in a hardware description language such as Verilog-A. Also, we perform VC-MTJ compact model parameters calibration based on measurement results.

We assume a single-domain MTJ structure where the three-dimensional dynamics of the free layer's magnetic moment $\vec{m} = \{m_x, m_y, m_z\}$, with $|m^2| = 1$, can be described via a LLG equation in the presence of an voltage-dependent effective field $\vec{H}_{eff}(V)$ [13].

where α is the material-dependent Gilbert damping factor, $\vec{m}$ is a unit vector in the direction of magnetization, and $\gamma`$ is the reduced gyromagnetic ratio. The first term in the equation (1) is responsible for precessional motion while the second term provides a damping torque that makes $\vec{m}$ align with $\vec{H}_{eff}$.

$$\frac{d\vec{m}}{dt} = -\gamma`\vec{m} \times \vec{H}_{eff} - \alpha\gamma`\vec{m} \times \left(\vec{m} \times \vec{H}_{eff}\right) \tag{1}$$

The effective magnetic field $\vec{H}_{eff}$ in the free layer of the MTJ is a function of the applied voltage across the device due to the VCMA effect. A quantitative analysis of voltage dependence of each component in $\vec{H}_{eff}$ allows extracting the critical voltage V_c, the minimum voltage that induces the voltage-driven precessional switching. In addition to the voltage amplitude across the device ($V_{MTJ} > V_c$), the pulse duration also plays a significant role in precessional reorientation. To achieve switching, the pulse needs to be removed when the magnetic moment achieves 180° reorientation. If the pulse duration is too long or too short, the magnetic moment may return to its initial state. Figure 7 illustrates the VCMA-induced precessional switching mechanism in the free layer of the MTJ.
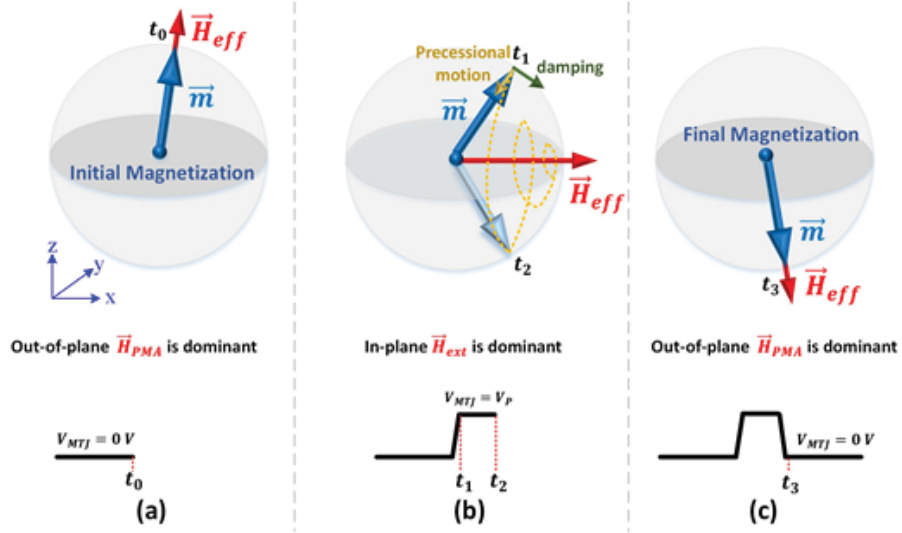
Figure 7: Illustration of the Voltage-Induced Precessional Switching Mechanism in the Free Layer of a Perpendicularly Magnetized MTJ

(a) Under zero electric bias condition ($V_{MTJ} = 0\,V$ at $t < t_0$), the free layer is aligned with the out-of-plane direction because the perpendicular magnetic anisotropy $\vec{H}_{PMA}$ is a dominant component in $\vec{H}^{\perp}_{k,eff}$. (b) When an applied voltage across the device reduces $\vec{H}^{\perp}_{k,eff}$ via the VCMA effect, the magnetic moment starts to precess around the in-plane direction. (c) If the width of the applied pulse is designed to coincide with half the precession period, a full 180° switching can be achieved. Note that voltage with opposite polarity cannot switch the device because it enhances $\vec{H}^{\perp}_{k,eff}$.

2.2 Calibration of Resistance-Area Product and TMR Ratio

Statistical MTJ resistance distributions and resistance-area (RA) product have been extracted as a function of the device diameter as shown in Figure 8. Typically, voltage-controlled MTJ devices have a relatively thick tunneling barrier (>1.5 nm), resulting in a high RA product. In the case of our measurement, the RA product is $650\ \Omega \cdot \mu m^2$. Also, to obtain high thermal stability, the size of MTJs in MeTCAM application is ranging from 80 nm to 120 nm, which in turn gives rise to MTJ resistance (R_P) ranging from 50 $k\Omega$ to 130 $k\Omega$.
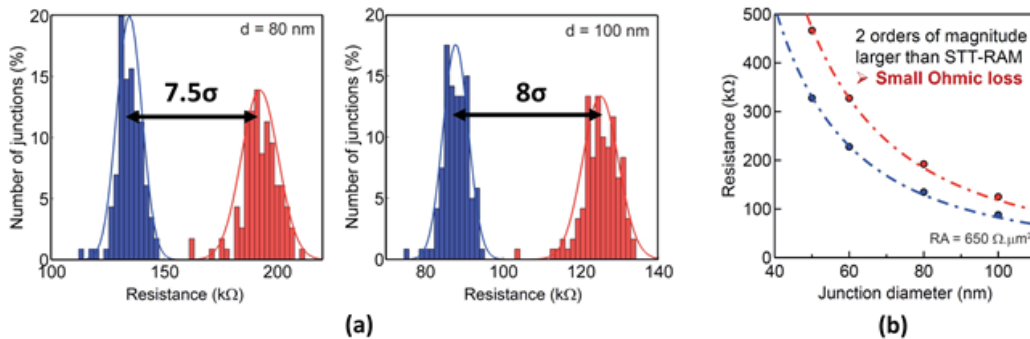

Figure 8: (a) MTJ Resistance Distributions and (b) Resistance and Area (RA) Product as a Function the Device Diameters

Due to the relatively thick tunnel barrier (MgO), VC-MTJs have a higher resistance compared to a conventional current-driven MTJ.

TMR ratio is defined by following equation,

$$\text{TMR} = \frac{R_{AP} - R_P}{R_P} \times 100 \tag{2}$$

Although TMR from our measurement shows 50%, it is possible to enhance it via device optimization. Hence, based on the measurement data, we determine the low and high resistive states of VC-MTJ compact model as either (i) $R_P = 50\ k\Omega$ and $R_{AP} = 150\ k\Omega$ (TMR=200%) or (ii) $R_P = 100\ k\Omega$ and $R_{AP} = 200\ k\Omega$ (TMR=100%).

2.3 Calibration of Voltage-Controlled Precessional Switching Speed

The switching time of VC-MTJ is equal to the half round trip time of precession motion of the free layer's magnetization. The precession speed is mainly determined by the in-plane component of an effective magnetic field $\vec{H}_{eff}$ in which the in-plane magnetic field originates from either a stray field from another magnetic layer of the device or an externally applied field. Figure 9(a) shows measured switching probability of VC-MTJ as a function of the applied pulse duration where the highest switching probability is observed between the pulse duration 0.8 ns and 1 ns. In the VC-MTJ compact model, the equivalent switching speed can be achieved by adjusting the in-plane magnetic field between 16 kA/m and 20 kA/m. This sub-nanosecond switching speed can be an advantage in a write (configuration) operation of MeTCAM application.
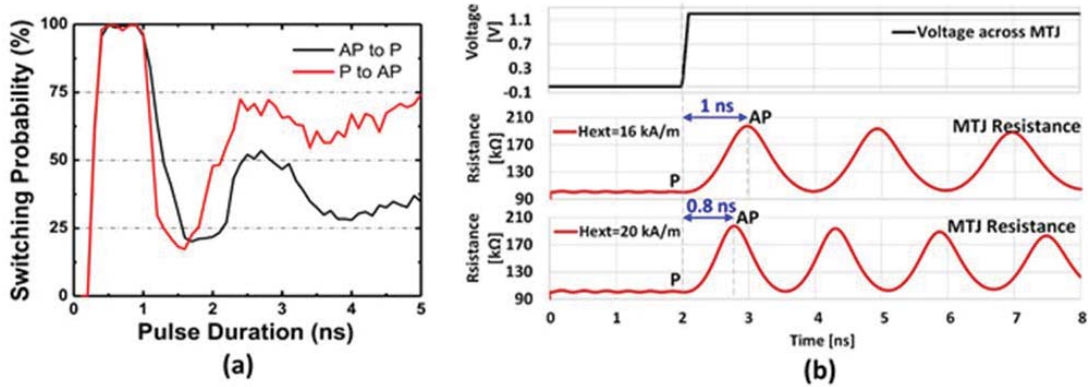
Figure 9: (a) Measured Probability of Precessional Voltage-Induced Switching in a Perpendicular MTJ, for both P to AP and AP to P Directions and (b) Transient Simulations for the In-Plane External Magnetic Field H_{ext} Dependence of the Switching Speed
(a) Note the oscillatory dependence of the write probability on the voltage pulse duration, which is a signature of the precessional write process. (b) As the H_{ext} increases, the switching speed increases

3. Spike-based TCAM Architecture using SRAM

3.1 Structural Optimization

The operation sequence of a TCAM includes enable search→match/mismatch comparison→detect output of the search results→return to initial state. These operations lead to three design aspects in the structure of a SRAM-based spiking TCAM cell:

1. Design of the comparison path: In the conventional TCAM cell, the comparison path is connected between the ML and ground, and becomes conducting when the cell is mismatch, leading to discharge of the ML. On the other hand, the spiking architecture accepts spikes as input and generates a post-cell spike when a match occurs. When the cell is a mismatch, no post-cell spike is generated. Thus, the comparison path should be conducting when a match occurs. Furthermore, for the smallest cell area configuration, the output polarity is inverted, leading to the need for a reversed comparison path.
2. Pre-charge and enable: In the conventional TCAM, the ML is pre-charged to high before a search operation. The search operation is enabled by the SL. For the spiking TCAM, the comparison operation is enabled when a spike is received (M_{EN}). At the end of the spike, the cell should return to its original state (M_{PRE}).
3. Design of the search path: The spike-propagating TCAM (SPTCAM) takes advantage of removing redundant searches to minimize energy, at the cost of a slightly lower search speed. To alleviate this issue, we need to minimize the delay of the search path. This can be achieved by minimizing capacitive charging during the search operation. In other words, the search path should pass through a minimal amount of capacitive loading, and nodes that can be determined before the spike is received should be computed early.

We investigate two cell designs that fulfill the above constraints, as shown in Figure 10. In Figure 10(a), the spike passes through the cell extremely fast and as the delay along the propagation path is minimized. On a match, nodes on the comparison path (L, R, and Nx) are already at their final values prior to receiving the spike. However, this structure potentially suffers from data-dependent noise with the search data is a mismatch. When the comparison path is cut-off, Nx is floating prior to receiving a spike. The search operation will thus be affected by the previous voltage on Nx. When the previous search is a match and the current search is a mismatch, Nx will be floating 0, and the output will slightly drop despite the comparison path being nonconducting.

The structure in Figure 10(b) trades a portion of speed and energy for higher reliability. While nodes L and R are evaluated after the spike arrives, nodes on the search path will be pre-charged and thus the output will not be affected from the previous search operation. This avoids the issue of data-dependent noise. We currently use this configuration for the evaluation of the scheme, however do not rule out the possibility of the design in Figure 10(a) as it is ~1.8x better in terms of speed and energy.

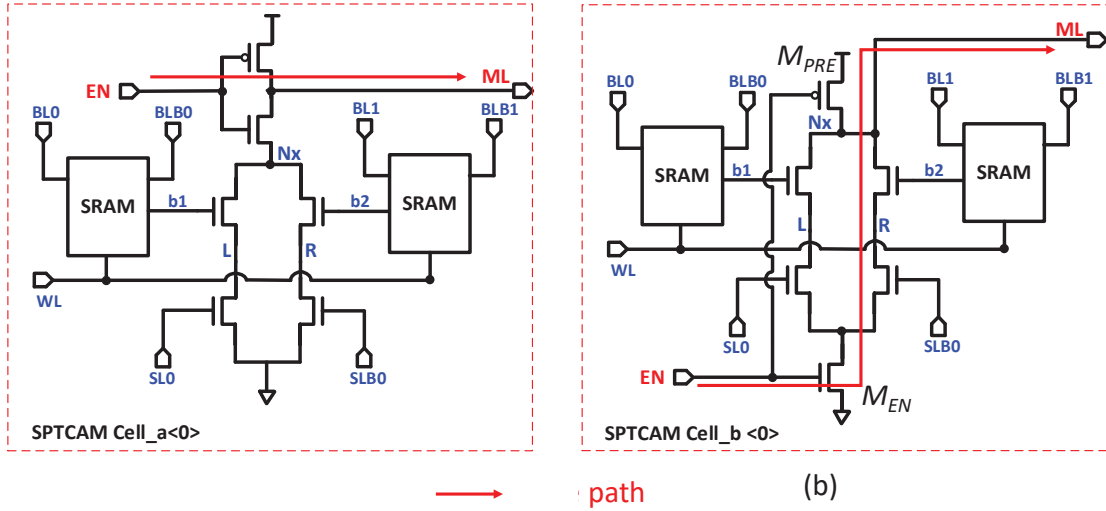Approved for public release; distribution is unlimited.

Figure 10: (a) High-Speed, Low-Energy Cell Structure and (b) Reliable Cell Structure
(a) The spike propagation path is minimized and internal nodes L and R are determined before the spike arrives. However, this structure suffers from data-dependent noise. (b) There will not be any data-dependent floating nodes along the search path. However, this comes at the cost of lower speed and increased energy consumption.

3.2 Performance Analysis

The key performance of a TCAM can be evaluated in terms of its speed (delay^{-1}) and its energy efficiency (energy/search)-1. A common figure of merit (FOM) is the energy-delay product (EDP, energy^{-1}delay^{-1}). We constructed a 32-bit, 64-bit, and 128-bit TCAM and analyzed these metrics for the conventional and the spiking structures. The delay is computed as the delay from the search enable to the output being detected. To find the average energy/search, we first simulate the delay and energy of different data patterns: in the conventional case, these include all match, 1-bit mismatch, to all miss; in the spiking architecture, they include all miss, miss at first bit, to miss at last bit and all match. The ML energy is calculated as the total energy consumed on the shared ML for the conventional case and each ML for the spike-propagation case. The SL energy is the energy consumed on the SL to input the search data for each search operation. We then compute the average energy consumption assuming a uniform distribution in the data (i.e. all patterns have equal possibility).

Figure 11 shows the metrics of the spiking structure compared to the conventional structure for different bit lengths. The spiking structure suffers from a ~8x longer delay than the conventional structure. However, it saves 27x~87x energy across different ML lengths. The energy saving is particularly pronounced when the ML length is long, in which most searches are redundant and eliminated by the spike-propagating structure. Thus, at a ML length of 128-bit, the overall FOM of the spike-propagating architecture is 7.5x larger than that of the conventional TCAM.
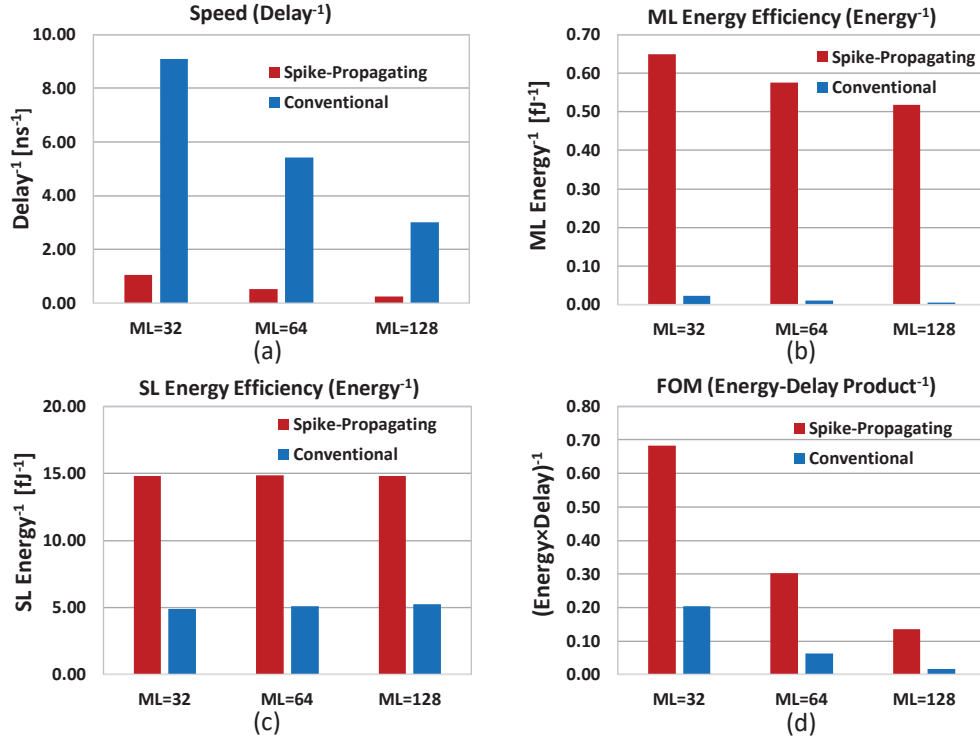
Figure 11: SPTCAM Performance Comparison with Conventional TCAM across different ML Lengths

(a) Speed, (b) ML energy efficiency, (c) SL energy efficiency, and (d) FOM (energy-delay product^{-1})

3.2.1 Process-Voltage-Temperature (PVT) Variation

We first identify the effect of global process variation on the performance metrics through simulation of each process corner. The variations are represented by two-letter designators, where the first letter refers to the n-type metal-oxide-semiconductor (NMOS) variation, and the second letter refers to the PMOS variation. In this naming convention, three variations exist: typical (T), fast (F) and slow (S), giving rise to five important corners: TT, FF, SS, SF, and FS. As shown in Figure 12, the FOM of the SPTCAM is especially good in SS since it enhances its low power advantage. This suggests that low-power processes benefit the SPTCAM. Conventional TCAM requires high speed, so optimum performance is achieved at the FF corner.
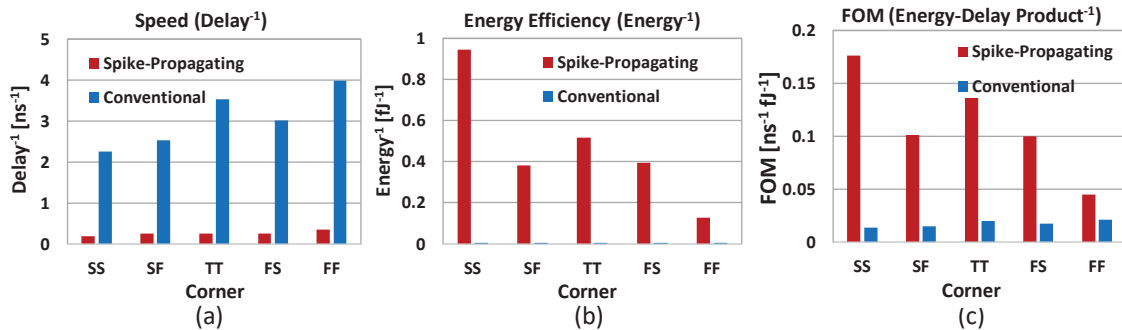

Figure 12: SPTCAM Performance Comparison with Conventional TCAM across different Process Corners

(a) Speed, (b) ML energy efficiency, and (c) FOM (energy-delay product^{-1})

12

We then inspect the effect of different voltages by sweeping the supply voltage from 0.6 V to 1.2 V with 0.2 V step, as shown in Figure 13. The nominal VDD of the process is 1V. As the supply voltage increases, the speed of both structure increase, and the energy consumption also rises. The search delay of the conventional structure is ~10x faster than the spike-propagating structure for a 128-bit ML due to the long propagation path, as shown in Figure 13(a). The average search energy on the ML of SPTCAM is 90x lower than that of conventional TCAM as shown in Figure 13(b). As a result, the EDP of SPTCAM is average 8.5x better than that of TCAM. The SPTCAM achieves the best EDP at VDD=0.6 V, while the conventional TCAM works best at the nominal VDD.

Figure 13: SPTCAM Performance Comparison with Conventional TCAM across different Supply Voltages
(a) Speed, (b) ML energy efficiency, and (c) FOM (energy-delay product^{-1})

Lastly, we investigate the effect of temperature variation on the performance of each structure. We address the temperature for standard benchmark cases, namely -40ºC, 25ºC, and 125ºC, as shown in Figure 14. At higher temperatures, performance degrades as both the delay and the energy consumption increases. The FOM of the spike-propagating structure suffers more at high temperatures, as the leakage energy begins to dominate search energy.
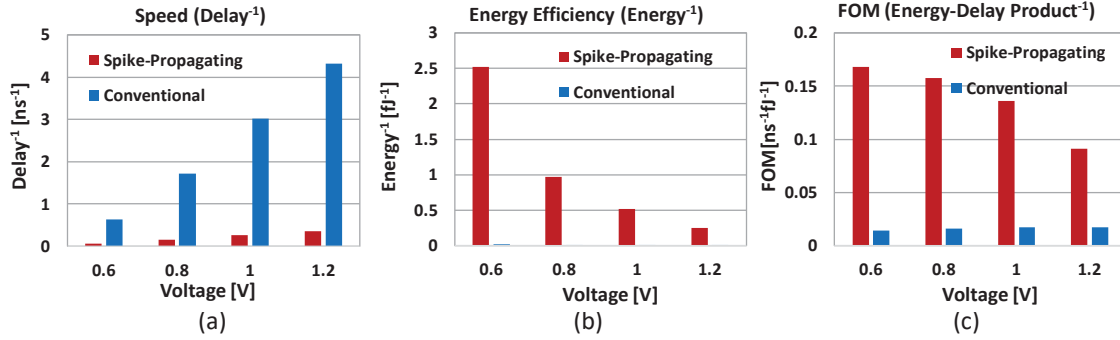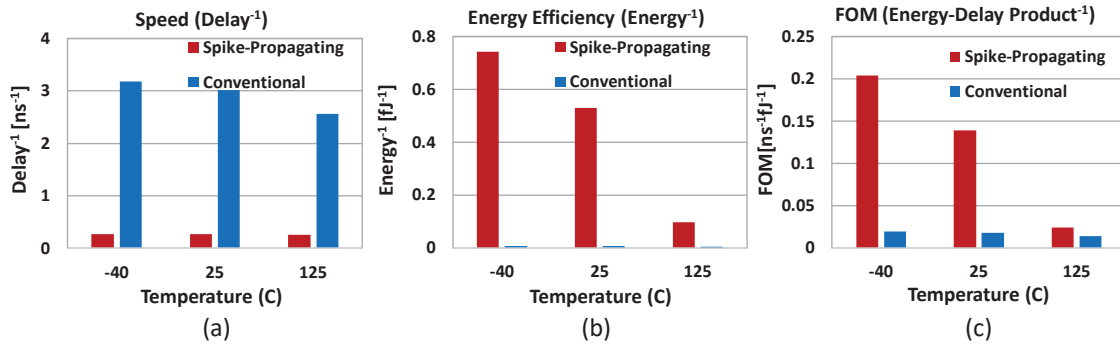

Figure 14: SPTCAM Performance Comparison with Conventional TCAM across different Temperatures
(a) Speed, (b) ML energy efficiency, and (c) FOM (energy-delay product^{-1})

3.2.2   Local Mismatch

The Monte Carlo (MC) method is a means of statistical evaluation of mathematical functions using random samples. Since it is impossible to completely avoid mismatches between components, the MC mismatch analysis provides insight into the effect of these variations. Random variables generate mismatch (i.e. channel length, width, etc.) in a device based on measured results for each trial. 1000 trials are executed to find the 3-sigma performance variation in both architectures. Figure 15 presents the result of the MC mismatch simulation of the conventional 128-bit TCAM where its mean and standard deviations are 329 ps and 12 ps, respectively. The maximum throughput of the conventional TCAM is limited by the longest delay (361 ps), as shown in Figure 15(a). For the spike-propagating structure, the maximum throughput is determined by the minimum spike width (Figure 15(b)) and delay (Figure 15(c)), which will need to cover variation of transistors. Spike width smaller than the variation may result in the spike being unidentifiable at the output. Delay smaller than the variation may cause spikes to collide. For reliable operation, the maximum operating frequency is the sum of the two distributions. This indicates that the minimum cycle for the spike-propagating architecture is thus 570ps.
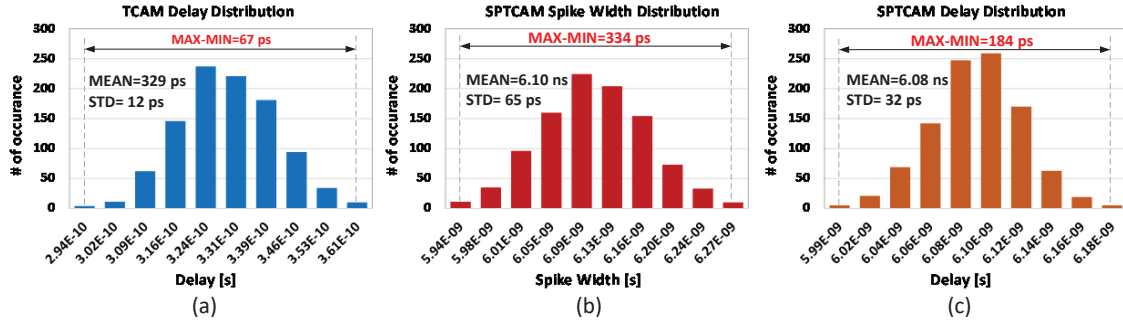
Figure 15: Local Mismatch Simulation for a 128-bit Conventional and the Spike-Propagating Structure
(a) Conventional TCAM delay distribution, (b) spike-propagating TCAM output spike width distribution, and (c) spike-propagating TCAM delay distribution.

For a non-pipelined architecture, the delay itself determines the throughput of the device. However, when the pipeline scheme is applied, the minimum cycle determines the throughput. By applying the pipeline scheme, our new FOM, defined as (throughput * energy efficiency) can be further improved to a 50x improvement over the conventional scheme.

4. MeTCAM Cell Design

4.1 Structural Analysis

For precise search operation, spikes received at each cell should be shaped such that the cell can distinguish match and mismatch. In other words, the potential at CE (See Figure 4(a)) should reach the threshold if the cell is a match and remain below the threshold otherwise. However, as the spike propagates along the search path, its shape will inevitably change due to the asymmetric slope, delay, and voltage range between the rising and falling edges. This change will accumulate along the search path and eventually cause the search operation to fail. As 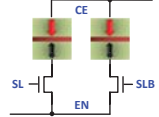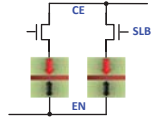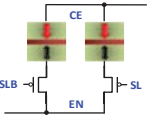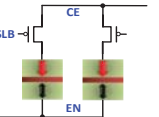such, we need to create different configurations of the MeTCAM cell and utilize a combination of different cell configurations to calibrate the spike shape along the spike propagation path.

To design the path of spike propagation, we analyze the delay, acceptable input spike shape for correct search operation, and post-cell spike duration for a variety of MeTCAM cell configurations. Two main configurations without increasing the MeTCAM cell area are discussed: the selection of transistor type (PMOS or NMOS) for M1/M2, and the placement of M1/M2 with respect to the VC-MTJs (M1/M2 connect to CE, or VC-MTJ connected to CE). These analyses are then carried out for different input spike polarities (positive and negative spikes). A summary of the analytical and quantitative results is shown in Table 2. The transistor type mainly affects rising/falling slope and CE voltage range. The location of transistors further manipulates the slope of one edge (but not the other) through source degeneration, where voltage drop across the VC-MTJ during the search operation causes the driving capability of the M1 and M2 to reduce.

Table 2. Delay, Post-Cell Spike Characteristics (t_{SPIKE_O}), and acceptable Input Spike (t_{SPIKE_I}) of different Cell Configurations when Stimulated by Positive and Negative Spikes

The delay and t_{SPIKE_O} values shown are simulated with input spike being in the center of the t_{SPIKE_I} range. However, they will slightly vary for different t_{SPIKE_I} and different input spike shapes

Cell Configuration	Rising (0->1)	Falling (1->0)	Response to pos. pulse	Response to neg. pulse
N	slow, with degeneration	fast	Delay : 127ps t_{SPIKE_O}* : -86ps t_{SPIKE_I}** : 130-230ps	Delay : 46ps t_{SPIKE_O} : +56ps t_{SPIKE_I} : 30-60ps
ZN	slow	Fast, with degeneration	Delay : 78ps t_{SPIKE_O} : -25ps t_{SPIKE_I} : 70-130ps	Delay : 65ps t_{SPIKE_O} : +6ps t_{SPIKE_I} : 50-110ps
P	fast	Slow, with degeneration	Delay : 44ps t_{SPIKE_O} : +133ps t_{SPIKE_I} : 30-50ps	Delay : 170ps t_{SPIKE_O} : -131ps t_{SPIKE_I} : 170-290ps
ZP	Fast, with degeneration	slow	Delay : 62ps t_{SPIKE_O} : +34ps t_{SPIKE_I} : 50-100ps	Delay : 106ps t_{SPIKE_O} : -38ps t_{SPIKE_I} : 100-150ps

*Duration of post-cell spike duration with respect to the input spike duration
** Range of the input spike duration for a cell to distinguish between match and mismatch

The delay of the first edge of the input spike determines the search delay of the cell. On the other hand, the rising/falling edge speed difference translates to a change in the spike shape. When the first edge has a longer delay then the second edge, the spike duration is shortened. Thus, the N/ZN (P/ZP) configuration reduce the spike duration for positive (negative) spikes. If the first edge of the spike experiences source degeneration, the post-cell spike is further shortened. As a result, the N/P (ZN/ZP) configurations shorten the spike duration more (less) significantly. Through combinations of these different configurations, the spike shape along the propagation path can be calibrated.

The slope of signal development, which is mainly determined by the location of the transistor, translates to the acceptable input pulse duration. The source degeneration decreases signal development in one direction, changing the required input pulse duration. The N (P) configuration thus has a significantly longer and wider input spike duration for a positive (negative) pulse compared to their ZN (ZP) counterparts.

4.2 Layout Extraction

We constructed the layout of each cell configuration to extract its parasitic capacitances for a more accurate simulation of its behavior in the physical chip. The area of each cell in 65nm technology is roughly $3um^2$ in 65nm technology, which is ~3x smaller compared to the conventional TCAM cell in the same technology. An illustration of the layout of a single cell is shown in Figure 16, with each node labeled according to Figure 4(a). The extracted parasitic capacitances show that the ZN/ZP configuration has a slightly larger capacitance on the CE node, as the MeRAMs contribute to its loading. On the other hand, the N/P configuration has a slightly larger capacitance on the EN node. SLB has a larger parasitic capacitance than SL since SLB is closer to the internal parts of the circuit, leading to an increased capacitance on its metal lines. A summary of the extracted parasitic results are shown in Table 3. Post-layout simulations of each cell are shown in Table 4.
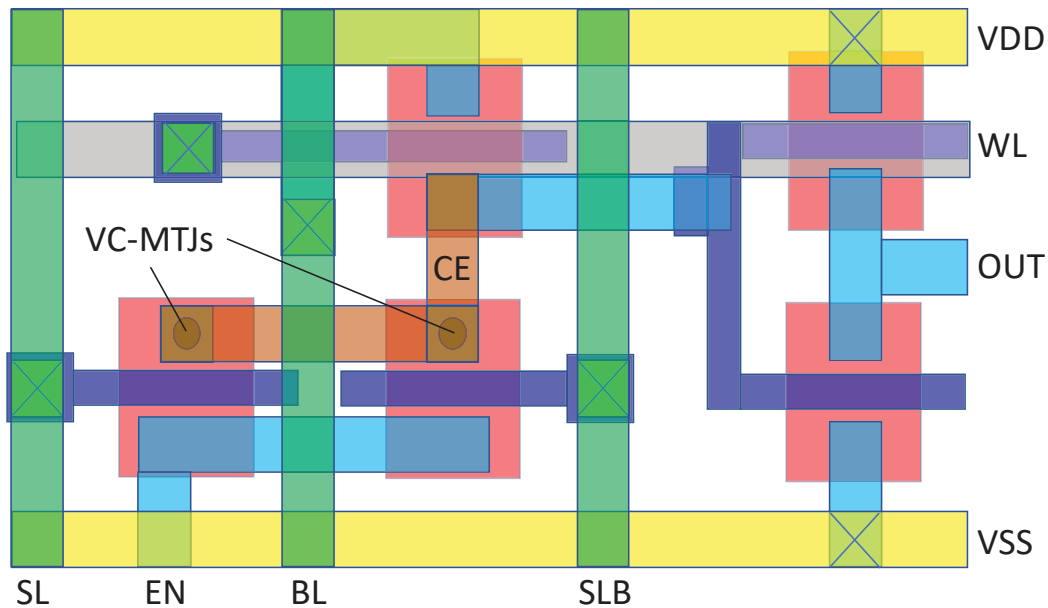
Figure 16: Illustration of the Layout of a MeTCAM Cell
The cell area occupies $3um^2$, while that of a conventional TCAM cell occupies around $9um^2$.

Table 3. Post-Layout Parasitics on each Node along the Search Path

Node	P	N	ZP	ZN
CE	0.54	0.54	0.51	0.51
EN	0.19	0.19	0.28	0.28
OUT	0.22	0.22	0.22	0.22
SL	0.2	0.2	0.2	0.2
SLB	0.34	0.34	0.34	0.34

Unit: fJ

Table 4. Post-Layout Characteristics of each Cell Configuration

Cell Configuration	Response to pos. pulse	Response to neg. pulse
N	Delay : 168ps t_{SPIKE_O}*: -117ps t_{SPIKE_I}**: 180-320ps	Delay : 61ps t_{SPIKE_O} : +53ps t_{SPIKE_I} : 30-80ps
ZN	Delay : 99ps t_{SPIKE_O} : -26ps t_{SPIKE_I} : 90-160ps	Delay : 81ps t_{SPIKE_O} : +7ps t_{SPIKE_I} : 70-130ps
P	Delay : 60ps t_{SPIKE_O} : +83ps t_{SPIKE_I} : 30-70ps	Delay : 228ps t_{SPIKE_O} : -170ps t_{SPIKE_I} : 240-390ps
ZP	Delay : 79ps t_{SPIKE_O} : +37ps t_{SPIKE_I} : 70-120ps	Delay : 135ps t_{SPIKE_O} : -72ps t_{SPIKE_I} : 130-200ps

5. MeTCAM Array Design

5.1 Search Path Construction

As mentioned earlier, the criteria for correct MeTCAM operation is that the post-cell spike duration of the Nth cell needs to be within the input pulse-width range of the $N+1^{th}$ cell. The post-layout simulations from Section 4.2 serve as design constraints and guidelines for constructing the search path. A variety of cell configurations are used to calibrate the spike shape as it propagates. A design example of a 16-bit spike-propagation path is shown in Figure 17.
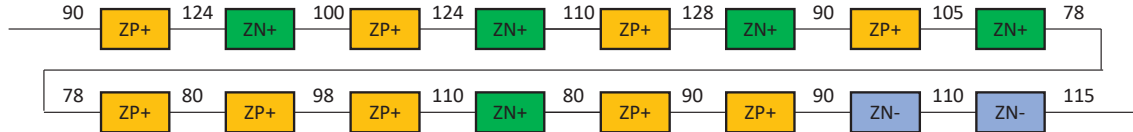
Figure 17: Example of a 16-bit Spike-Propagation Path

The terminology is (cell configuration-input polarity) (i.e. ZP+ represents a ZP configuration with a positive input pulse). The simulated spike duration after each cell is shown on the connection between each MeTCAM cell.

We then construct a 64-bit MeTCAM array and verify its operation through simulating patterns of all-match and mismatch at each point along the search path. The 64-bit MeTCAM array was based on the 16-bit arrays, with modifications along the search path where the spike duration falls out of range. Figure 18 shows the simulated waveform of each post-cell spike along the search path for (a) all match, (b) a mismatch at the 15th bit, (c) a mismatch at the 31st bit, (d) a mismatch at the 47th bit, and (e) a mismatch at the 63rd bit.

Figure 18: Simulated Waveforms along the Search Path for various Search Data Patterns

5.2 Pipeline and Optimization
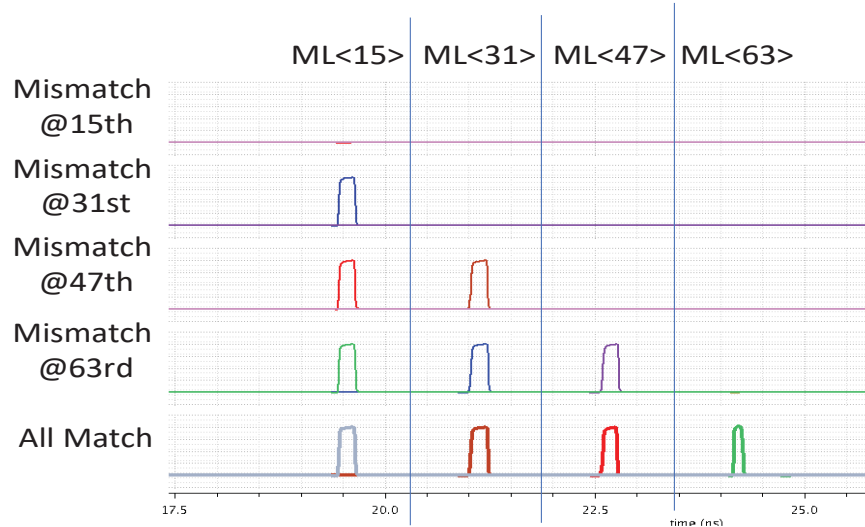
We show applicability of the pipeline scheme by conducting search operations with a frequency greater than the total search path delay. For the 64-bit ML, the delay is ~6.4ns. With the pipeline scheme, search operation can be conducted with a cycle of 1ns. Note that, at high search frequencies, the characteristics of each cell configuration shown in Table 4 will change. For example, the P cell becomes easier to stimulate.
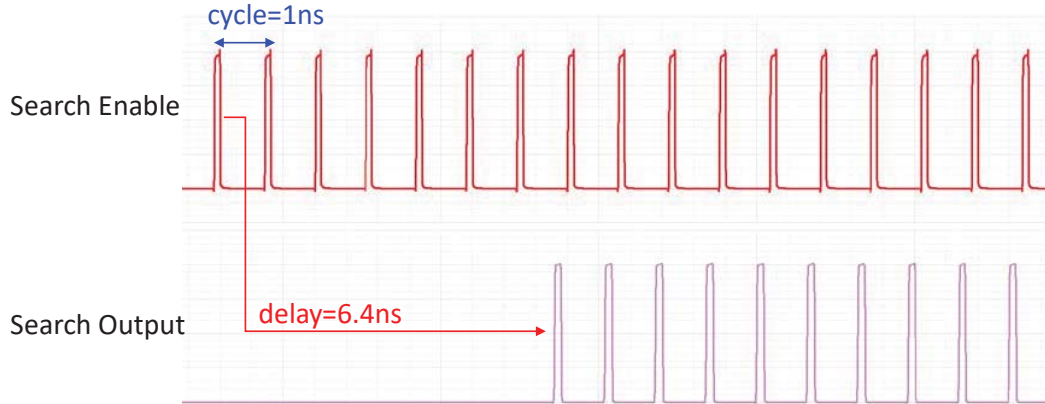
Figure 19: Applicability of Pipeline Scheme for a 64-bit MeTCAM, where the Search Cycle Time can be as fast as 1ns despite the Intrinsic Delay being 6.4ns

Furthermore, we can use the cell characteristics results to optimize the search path depending on the target specifications. For maximum area efficiency, the spikes should interleave between positive and negative spikes, so that the buffer size can be reduced. For optimal latency, the total delay on the search path should be minimized; for maximum throughput the spike-duration of each stage should be as short as possible. It is beneficial to have a relatively long spike at the last stage for better detection.

6. Technical Accomplishments

Task 1: Design and simulation environment setup.
    (a) Setup the design platform on virtuoso with the commercial TSMC 65nm process design kit (PDK) for mixed-signal circuit simulation. Obtained the North Carolina State University 40nm and 15nm Fin field-effect transistor (FinFET) PDK for evaluation in highly advanced technologies.
    (b) Completed the Verilog-A based compact VC-MTJ model compatible with the design environment. The model has been calibrated with the most recent experimental results on VC-MTJ devices.

Task 2: Design of MeTCAM cell and architecture (schematic level) and verification of the circuits based on the Spectre circuit simulation.
    (a) Constructed and optimized the SRAM-based spike-propagating architecture and verified its performance across global PVT variations and local mismatch variations. Results showed a ~50x improvement in energy efficiency-throughput product.
    (b) Designed various MeTCAM configurations and extracted characteristics of each cell variety. Constructed the MeTCAM cell layout and performed post-layout simulation for accurate physical-chip level evaluation.
    (c) Identified and investigated the design challenges of a MeTCAM array. Then designed a 64-bit MeTCAM array and verified its functionality, as well as applicability of the pipeline scheme

Task 3: Physical chip layout and extraction of GDSII file.
    (a) Drew the layout of various MeTCAM cell configurations and performed verifications including DRC, LVS, and PEX. The post-layout extracted results have been incorporated into design process.

TASK 4: VC-MTJ devices fabrication via back-end-of-line (BEOL) process.
    (a) Fabricated high-VCMA VC-MTJs, with junction dimensions ranging from 50nm to 100 nm.
    (b) Extracted statistical distributions on the switching speed and RA product of our fabricated VC-MTJ devices. These values have been incorporated into our compact model and used in circuit simulation

Approved for public release; distribution is unlimited.

7. References

[1]   Jinn-Shyan Wang, Chao-Ching Wang, and Chingwei Yeh, "TCAM for IP-Address Lookup Using Tree-style AND-type Match Lines and Segmented Search Lines," in *2006 IEEE International Solid State Circuits Conference - Digest of Technical Papers*, 2006, pp. 577-586.

[2]   A. Igor, C. Trevis, and A. Sheikholeslami, "A ternary content-addressable memory (TCAM) based on 4T static storage and including a current-race sensing scheme," *IEEE J. Solid-State Circuits*, vol. 38, no. 1, pp. 155-158, Jan. 2003.

[3]   S. Matsunaga, A. Katsumata, M. Natsui, T. Endoh, H. Ohno, and T. Hanyu, "Design of a Nine-Transistor/Two-Magnetic-Tunnel-Junction-Cell-Based Low-Energy Nonvolatile Ternary Content-Addressable Memory," *Jpn. J. Appl. Phys.*, vol. 51, no. 2, p. 02BM06, Feb. 2012.

[4]   J. Li, R. K. Montoye, M. Ishii, and L. Chang, "1 Mb 0.41 μm^2 2T-2R Cell Nonvolatile TCAM With Two-Bit Encoding and Clocked Self-Referenced Sensing," *IEEE J. Solid-State Circuits*, vol. 49, no. 4, pp. 896-907, Apr. 2014.

[5]   L. Zheng, S. Shin, and S.-M. S. Kang, "Memristors-based Ternary Content Addressable Memory (mTCAM)," in *2014 IEEE International Symposium on Circuits and Systems (ISCAS)*, 2014, pp. 2253-2256.

[6]   S. Ikeda, K. Miura, H. Yamamoto, K. Mizunuma, H. D. Gan, M. Endo, S. Kanai, J. Hayakawa, F. Matsukura, and H. Ohno, "A perpendicular-anisotropy CoFeB–MgO magnetic tunnel junction," *Nat. Mater.*, vol. 9, no. 9, pp. 721-724, 2010.

[7]   P. Wang, W. Zhang, R. Joshi, R. Kanj, and Y. Chen, "A thermal and process variation aware MTJ switching model and its applications in soft error analysis," in *Proceedings of the International Conference on Computer-Aided Design - ICCAD '12*, 2012, p. 720.

[8]   G. D. Panagopoulos, C. Augustine, and K. Roy, "Physics-Based SPICE-Compatible Compact Model for Simulating Hybrid MTJ/CMOS Circuits," *IEEE Trans. Electron Devices*, vol. 60, no. 9, pp. 2808-2814, Sep. 2013.

[9]   G. D. Demin, E. E. Gusev, A. F. Popkov, P. A. Stepanov, and N. A. Djuzhev, "Compact HSPICE model of magnetic tunnel junction based on voltage-driven spin-transfer torque," in *2016 International Siberian Conference on Control and Communications (SIBCON)*, 2016, pp. 1-6.

[10]   A. S. Roy, A. Sarkar, and S. P. Mudanai, "Compact Modeling of Magnetic Tunneling Junctions," *IEEE Trans. Electron Devices*, vol. 63, no. 2, pp. 652-658, Feb. 2016.

[11]   S. Sharmin, A. Jaiswal, and K. Roy, "Modeling and Design Space Exploration for Bit-Cells Based on Voltage-Assisted Switching of Magnetic Tunnel Junctions," *IEEE Trans. Electron Devices*, vol. 63, no. 9, pp. 3493-3500, Sep. 2016.

[12]   W. Kang, Y. Ran, Y. Zhang, W. Lv, and W. Zhao, "Modeling and Exploration of the Voltage-Controlled Magnetic Anisotropy Effect for the Next-Generation Low-Power and High-Speed MRAM Applications," *IEEE Trans. Nanotechnol.*, vol. 16, no. 3, pp. 387-395, May 2017.

[13]   L. D. Landau and E. M. Lifshits, "On the theory of the dispersion of magnetic permeability in ferromagnetic bodies," vol. 8, pp. 153-169, Jan. 1935.

List of Abbreviations, Acronyms, and Symbols

Acronym	Description
AP	Anti-Parallel
BEOL	Back-End-Of-Line
BL	Bit Line
CAM	Content Addressable Memory
CE	Center
CMOS	Complementary Metal-Oxide-Semiconductor
DARPA	Defense Advanced Research Agency
EDP	Energy-Delay Product
EN	Enable
FinFET	Fin Field-Effect Transistor
FOM	Figure of Merit
IP	Internet Protocol
LLG	Landau-Lifshitz-Gilbert
MC	Monte Carlo
MeRAM	Magneto-electric Random Access Memory
MeTCAM	Magneto-Electric Ternary Content Addressable Memory
ML	Match Lines
MRAM	Magneto-resistive Random Access Memory
MTJ	Magnetic Tunnel Junction
NMOS	N-type Metal-Oxide-Semiconductor
P	Parallel
PCRAM	Phase-Change Random Access Memory
PDK	Process Design Kit
PMOS	P-type Metal-Oxide-Semiconductor
PVT	Process-Voltage-Temperature
RA	Resistance-Area
RAM	Random Access Memory
RC	Resistive-Capacitive
ReRAM	Resistive Random Access Memory
SL	Search Lines
SPTCAM	Spike-Propagating Ternary Content Addressable Memory
SRAM	Static Random Access Memory
STT-RAM	Spin-Transfer Random Access Memory
TCAM	Ternary Content Addressable Memory
TMR	Tunneling Magneto-Resistance
VCMA	Voltage-Controlled Magnetic Anisotropy
VC-MTJ	Voltage-Controlled Magnetic Tunnel Junction